Effects of Initial Static Shear Stress and Grain Shape on Liquefaction of Saturated Nanjing Sand

ZHUANG Haiyang[1*], *PAN Shuxuan*[1], *LIU Qifei*[1], *YU Xu*[2]

1. Institute of Geotechnical Engineering, Nanjing Tech University, Nanjing 210009, P.R. China;
2. School of Architecture Engineering, Nanjing Institute of Technology, Nanjing 211167, P.R. China

(Received 5 April 2020; revised 6 July 2020; accepted 12 July 2020)

Abstract: This paper mainly investigates the effects of initial static shear stress and grain shape on the liquefaction induced large deformation of saturated sand under torsional shear. Nanjing sand, mainly composed of platy grains, is tested with different initial static shear stress ratio (SSR) using a hollow column torsional shear apparatus. The tests find that the saturated Nanjing sand reaches full liquefaction under the superposition of initial static shear stress and cyclic stress for both stress reversal and non-reversal cases. However, it requires a large number of loading cycles to reach full liquefaction if stress reversal does not occur. With increasing the initial static stress, the large deformation of the Nanjing sand should mainly induced by the cyclic liquefaction firstly under a smaller initial shear stress, and then it should be induced by the residual deformation failure. The critical point occurs approximately when the initial shear stress is close to the amplitude of the cyclic shear stress. Meanwhile, it shows that grain angularity increases the liquefaction resistance when the initial static shear stress is zero. A small initial static shear stress causes the larger loss of liquefaction resistance for angular sand than rounded sand. At a high initial SSR, the angular sand is more resistant to the large residual deformation failure than the rounded sand.

Key words: Nanjing sand; liquefaction; initial shear stress; grain shape; residual deformation failure

CLC number: TU435; TU441 **Document code:** A **Article ID:** 1005-1120(2021)01-0044-13

0 Introduction

Liquefaction induced lateral ground deformation and the consequent damage to subsurface or above ground structures have been observed and documented during previous earthquakes. For example, Hamada et al.[1] documented that the lateral ground displacement induced by liquefaction during the 1964 Niigata earthquake reached several meters and caused severe damage to buildings, bridges, retaining structures and buried pipelines. Liquefaction induced lateral ground deformation has received intensive attention in academia in recent decades. General investigation methods include compilation and study of case histories[2-3], shaking table tests at *g* and in the centrifuge[4-7], small specimen laboratory tests[8-11], and analytical and numerical models[12-13]. Among the various methods, laboratory tests serve as a fundamental tool to explore the mechanism of the cyclic response of sands, providing insights into the mechanics behind liquefaction-induced lateral spread. Typical laboratory tests include triaxial tests[8-9,14], simple shear tests[15-16], and torsional shear tests[17-18].

Early studies applied triaxial apparatus to investigate the mechanism of liquefaction and the factors affecting the occurrence and consequence of liquefaction[8-10]. Under cyclic undrained loading, liquefaction can occur either as a strain softening response due to the loss of shear strength or cyclic mobility. The strain softening response generally occurs on relatively loose sand with contractive behavior. The

*Corresponding author, E-mail address: zhuang7802@163.com.

How to cite this article: ZHUANG Haiyang, PAN Shuxuan, LIU Qifei, et al. Effects of initial static shear stress and grain shape on liquefaction of saturated Nanjing sand[J]. Transactions of Nanjing University of Aeronautics and Astronautics, 2021, 38(1): 44-56.

http://dx.doi.org/10.16356/j.1005-1120.2021.01.004

cyclic mobility occurs on sand with a wide range of relative density with dilative behavior[19-20]. The cyclic response of sand is affected by many factors, such as the physical properties of the sand, including relative density, gradation, fines content, and grain shape, etc., specimen preparation methods, and loading path[21]. Among these factors, the static shear stress attracted intensive attention due to the fact that natural soils often sustain static shear stress before earthquakes due to anisotropic consolidation or ground surface inclination. Lee and Seed[8] and Seed[22] found that the initial static shear stress increases the cyclic strength of sand. Vaid and Chern[23] showed that the static shear stress can either increase or decrease the cyclic strength dependent on the relative density of the specimen, magnitude of static shear, and definition of liquefaction resistance. Recent work by Yang and Sze[24] and Yang and Pan[11] showed that there was a critical initial shear stress ratio (SSR), below which the static shear stress is beneficial to the liquefaction resistance while above which the static shear stress is detrimental to the liquefaction resistance.

Current procedures for estimating liquefied strength are mainly based on laboratory testing. However, due to the mechanical limitations, the shear strain is limited to 10%—20% during the triaxial tests. Although simple shear apparatus can apply a much higher strain than the triaxial ones, it can only be applied to the shear stress on the fixed plane directly instead of through the differential axial and circumferential stress as applied during the triaxial tests. As a result, Yoshimi and Oh-oka[17] conducted the ring shear tests to investigate the effects of static shear on the liquefaction resistance and found that the static shear decreased the cyclic strength of sand. They also found that it required shear stress reversal to trigger liquefaction and to develop significant cyclic shear strain. Meanwhile, Vaid and Liam[15] performed simple shear tests to investigate the cyclic behavior of Ottawa sand. They also found that the static shear stress could either increase or decrease the liquefaction resistance dependent on the relative density of the sand, the magnitude of the initial static shear and the shear strain level. To the above opinion, Chiaro et al.[18] performed a series of undrained cyclic torsional shear tests using a modified torsional shear apparatus that was capable of achieving a double amplitude of shear strain up to 100%, and investigated the effects of static shear stresses on the post-liquefaction deformation of Toyoura sand which was primarily composed of rounded grains.

To the effect of grain angularity on the soil liquefaction, it has been recognized as a major impact factor on the shear strength of cohesionless soils. Early study by Koerner[25] found that the angular particles had a better interlocking than the rounded ones and resulted in a higher internal frictional angle of soils. Study on the effects of soil angularity on the liquefaction resistance of cohesion soils is relatively limited. Ishibashi et al.[26] found that the grain angularity played an important role during pore-pressure buildup, and sand composed of angular grains was more resistant to liquefaction than sand composed of rounded grains. Vaid et al.[27] found that at same relative densities, angular sand was more resistant to liquefaction at lower confining pressures but less resistant at higher confining pressures than rounded sand, and for a given increase in confining pressure, angular sand suffered a larger loss in resistance to liquefaction than rounded sand. The above studies have mainly been completed by indoor tests. Meanwhile, the effect of grain angularity on the sand liquefaction can be also investigated by the discrete element method (DEM), which have explained the micromechanics of sand liquefactions under different grain angularity[28-29].

This paper investigates the liquefaction induced lateral deformation of Nanjing sand during torsional shear tests, focusing on the effect of initial static shear stress on the cyclic strain accumulation during torsional shear since the Nanjing sand is mainly composed of platy grains. The testing results are preliminarily compared with those from Toyoura sand composed mainly of rounded grains to explore the impact of grain shape on the resistance to cyclic strain accumulation during liquefaction.

1 Testing Apparatus and Materials

1.1 Testing apparatus

Fig.1 shows the dynamic hollow cylinder apparatus (HCA) employed in this paper. It consists of a pressure chamber, a servo host system, a hydraulic servo controlled loading system, an analog and digital signal collection system, and a personal computer (PC). Fig.2 shows that the HCA can apply to four loads on a specimen along four directions. They are axial force (W), torque (M_T), internal confining pressure (P_i), and external confining pressure (P_o). P_i and P_o are the hydrostatic pressures exerted on the rubber membranes.

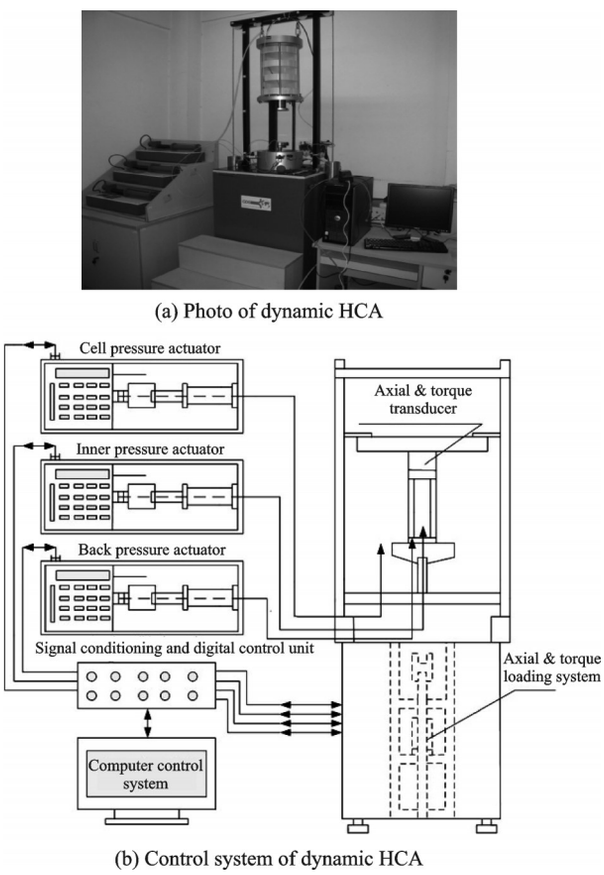

(a) Photo of dynamic HCA

(b) Control system of dynamic HCA

Fig.1 Photo of dynamic HCA and its control system

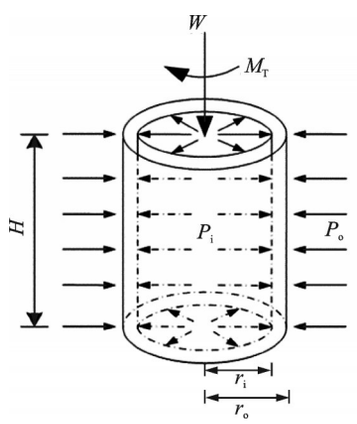

Fig.2 Loading directions of four different loads

Two servo-motors are used in the HCA. One controls the axial (vertical) movement through an actuator installed on the base of the cell, and the other controls the torsional movement. The torque is exerted by the rotation of the same ram that imposes the vertical force[30]. The vertical force and torque are measured by an internal submersible transducer. The vertical displacement and rotation of the specimen are measured using high-quality LVDTs mounted directly on the loading ram. Dynamic capacity is required to generate 10 kN axial load, 100 N·m torque, ±40 mm displacement, and unlimited degrees of rotation. The maximum loading frequency is 5 Hz. The measurement error of the vertical load, the torque, and the vertical and the rotational displacement are smaller than 0.1% FS, 0.11% FS, 0.15% FS, and 0.057% FS, respectively, where FS is the full-scale measurement range. The transducer resolutions of the vertical load, the torque, and the vertical and the rotational displacement are smaller than 0.7 N, 0.008 N·m, 1 μm, and 0.000 11°.

1.2 Physical properties of Nanjing sand

The Nanjing sand was borrowed from the Jianye area in Nanjing, southeast of China, which is a recent river deposit in the Yangzi river delta area. Fig.3 shows the gradation curve of the Nanjing sand. It is uniformly distributed with a mean particle size of 0.17 mm and fines content of 0.9%. It is classified as poorly graded fine sand based on the ASTM D2487-00 classification system. Table 1 lists the main physical properties of the Nanjing

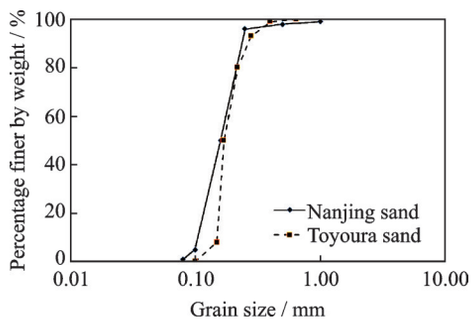

Fig.3 Gradation curves of Nanjing sand and Toyoura sand

Table 1 Physical parameters of Nanjing sand and Toyoura sand

Material	Specific gravity G_S	Mean diameter D_{50}/mm	Relative density D_r/%	Fines content/%	Max void ratio e_{max}	Min void ratio e_{min}
Toyoura sand	2.656	0.16	44—48	0.1	0.992	0.632
Nanjing sand	2.700	0.17	42.8—45.9	0.9	1.140	0.620

sand. A series of studies have been conducted on the physical properties of the Nanjing sand[30]. The studies show that the Nanjing sand is primarily composed of platy grains. Fig.4 shows the sand grains under microscope. Chiaro et al.[18] conducted a comprehensive study on the liquefaction and post-liquefaction behaviors of Toyoura sand that is mainly composed of rounded grains, which have similar grain size distribution and physical parameters but different grain shapes, as shown in Table 1. The grain size distribution, physical parameters, and grains of the Toyoura sand are shown in Fig.3, Table 1, and Fig.4, for comparison. As such, it provides an excellent opportunity to explore the effect of grain shape on the liquefaction and post-liquefaction behaviors of sand by comparing the testing results of the Nanjing sand with those of the Toyoura sand.

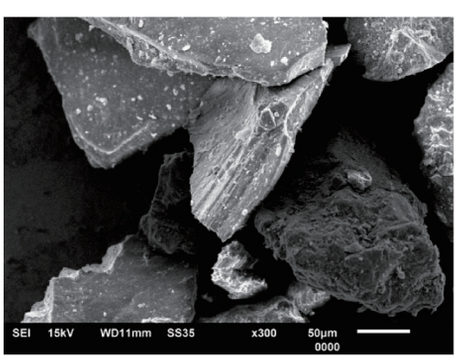

(a) Nanjing sand

(b) Toyoura sand

Fig.4 Sand grains under microscope

1.3 Specimen preparation and testing procedure

The specimens were prepared in a hollow cylindrical mold with an inner diameter of 60 mm, outer diameter of 100 mm, and height of 200 mm. The air-dried Nanjing sand was poured into the mold through a funnel by using the dry deposition method[31]. To achieve the desired relative density, the specimen was equally divided into eight sublayers. The dried sands were then placed into a specimen preparation mold. Each sublayer was placed into the mold using a funnel whose bottom was near the surface of a ready-made sublayer to alleviate the gravity effect of sands. To establish good contact between the two sublayers, we coarsely scratched the surface of a ready-made sublayer before adding the next sublayer. The specimen preparation process in this paper is shown in Fig.5.

All specimens were saturated in three stages. In the first stage, the specimens were flushed with carbon dioxide gas for a quarter. In the second stage, the de-aired water was flushed from

(a) Fixing of inner and outer membranes

(b) Pouring of dried sand into mold in eight layers

(c) Compacting of each layer to desired relative density

(d) Completion of soil compacting

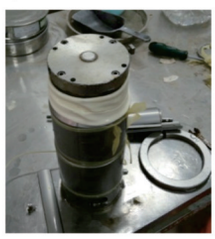

(e) Packaging of soil sample

Fig.5 Specimen preparation process

the bottom of the specimen toward the top until no more air escaped from the top of the specimen while the specimen was subjected to an effective confining pressure of 20—30 kPa. In the third stage, the specimens were saturated under a back-pressure of 200 kPa to achieve a pore pressure parameter B of 0.95. The specimens were then isotopically consolidated by increasing the effective stress state up to the expected values provided in Table 2. After isotropic consolidation, the stress state was modified by applying a drained monotonic torsional shear stress of up to a specified initial static shear stress shown in Table 2. Finally, undrained cyclic torsional loading was applied at a constant double amplitude until the double-amplitude shear strain reached 100% with controlled stress. Fig.5 shows the specimen preparation process.

Table 2 Testing parameters and results

Test No.	D_r/%	P_o'/kPa	CSR[1]	τ_{max}/kPa	τ_{min}/kPa	τ_{sta}/kPa	SSR[2]	Loading pattern	N_{IL}	$N_{7.5}$	N_{20}	N_{30}	N_{40}	N_{50}	N_{60}	N_{70}	N_{80}
1	44.3	80	0.3125	25	−25	0	0	RE[3]	1.6	1	3	8	12	18			
2	45.2	100	0.25	25	−25	0	0	RE	2.6	2	8	20	33	43			
3	45.4	120	0.208	25	−25	0	0	RE	5.6	5	14	24	36	47			
4	45.8	150	0.167	25	−25	0	0	RE	22	20	26	36	42	51			
5	42.8	100	0.14	14	−14	0	0	RE	85	85	92	101	108	115			
6	43.6	100	0.18	18	−18	0	0	RE	47	46	57	70	80	88			
7	44.1	100	0.3	30	−30	0	0	RE	1.6	1	3.5	9.3	19	31			
8	44.3	100	0.18	21	−15	3	0.03	RE	9	9	13	20	28	42	53		
9	43.1	100	0.18	24	−12	6	0.06	RE	8	6	9	14	18	21	25	31	
10	44.7	100	0.18	28	−8	10	0.1	RE	6	5	8	13	17	20	23	26	29
11	44.2	100	0.18	32	−4	14	0.14	RE	4	4	5	7	9	12	13	15	16
12	45.6	100	0.18	36	0	18	0.18	IN[4]	12	11	12	20	24	27	29	31	32
13	45.1	100	0.18	40	4	22	0.22	NR[5]	45	16	41	53	62	85			
14	45.4	100	0.18	45	9	27	0.27	NR	90	14	70	89	96	103			
15	54.3	100	0.18	18	−18	0	0	RE	59	59	73	92					
16	54.2	100	0.18	21	−15	3	0.03	RE	19	19	26	45	137				
17	53.1	100	0.18	24	−12	6	0.06	RE	16	16	19	27	41	66			
18	53.9	100	0.18	28	−8	10	0.1	RE	13	13	16	20	22	25	29	31	
19	54.2	100	0.18	32	−4	14	0.14	RE	7	7	13	16	18	21	24	27	29
20	55.6	100	0.18	36	0	18	0.18	IN	9	8	16	20	25	32	39	46	51
21	55.4	100	0.18	40	4	22	0.22	NR	66	22	49	56	62	67	72	76	
22	55.9	100	0.18	45	9	27	0.27	NR	420	32	301	401	422	430	436		

Note: (1) CSR: Cyclic stress ratio calculated as τ_{max}/P_o'; (2) SSR: Shear stress ratio calculated as τ_{sta}/P_o'; (3) RE: Stress reversal loading; (4) IN: Intermediate loading; (5) NR: Stress non-reversal loading.

Three patterns of cyclic loading, i.e. stress reversal, intermediate and non-reversal, as defined by Hyodo et al.[32], were employed. During the stress reversal loading, the direction of shear stress after the superposition of the initial static (τ_s) and cyclic shear stress (τ_d) was reversed from positive ($\tau_{max}=\tau_s+\tau_d>0$) to negative ($\tau_{min}=\tau_s-\tau_d<0$) or vice versa. During the intermediate loading, the minimum stress touched zero ($\tau_{min}=\tau_s-\tau_d=0$). During the stress non-reversal loading, the direction of shear stress remained positive ($\tau_{min}=\tau_s-\tau_d>0$).

The testing parameters are summarized in Table 2. Four series and 22 specimens were tested. The first and the second series were tested with zero static shear stress but different effective confining stresses and amplitudes of cyclic stress. The third and the fourth series were tested with constant effective confining stress but different relative densities and amplitudes of cyclic stress.

2 Test Results

2.1 Correction for membrane force

The rubber membranes attached to the inner and outer circumferential surface of the sand specimen deform during the rotation of specimen cap and share part of shear stress with the specimen. Previous studies (e.g., Chiaro et al.[18]) show that when the shear strain is large, the part of shear stress taken by the membranes becomes significant and should be subtracted from the total shear stress to obtain the net shear stress on the specimen. Chiaro et al.[18] introduced the following equation based on linear elasticity theory to calculate the membrane stress

$$\tau_m = \frac{t_m E_m (r_o^3 + r_i^3)\theta}{(r_o^3 - r_i^3)h} \tag{1}$$

where θ is the rotational angle of the top cap measured by an external potentiometer, r_o and r_i are the outer and the inner radii of the specimen, respectively, h is the height of the specimen, and t_m and E_m are the thickness (0.1 mm) and Young's modulus (1 492 kPa) of the membrane, respectively. The values of t_m and E_m are provided by the manufacturer.

To verify Eq.(1), we performed a test by pouring water between the inner and outer membranes and shearing the water specimen cyclically. Since water cannot sustain shear stress, all the shear stress was taken by the membranes. Fig.6 shows the relation between the shear strain and the stress during the torsional deformation of the membranes. In Fig.6, when the single-amplitude shear strain was smaller than 20%, the measured shear strain vs. stress curve was very close to the linear relation specified by Eq.(1); when the shear strain level exceeded 20%, the measured stress was smaller than the predicted stress. The difference was probably due to the buckling of the membranes. A regression was developed for the shear stress vs. strain relationship, as shown in Fig.6. This regression was used to correct the shear stress in this paper. Fig.7 shows an example of the stress correction based on the test on the Nanjing sand. In Fig.7, when the amplitude of the shear strain was small, the effect of the membrane force was barely perceptible. With increasing shear strain amplitude, the effect of the membrane force becomes significant and should be corrected.

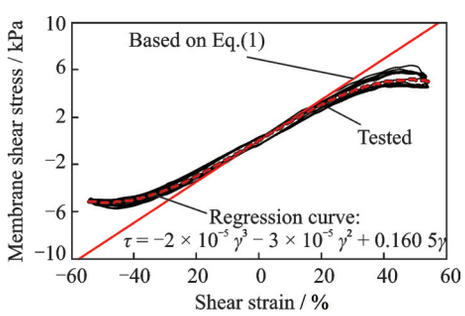

Fig.6 Shear stress vs. strain of water specimen

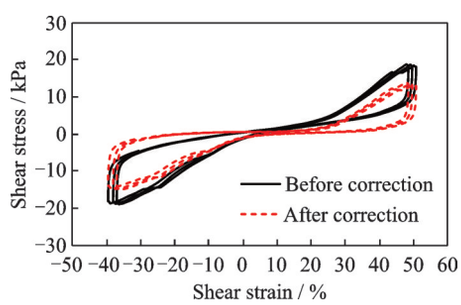

Fig.7 Example of shear stress correction

It should be explained that all the tests in this paper can only be loaded with the constant amplitude of torque under the limit of test apparatus. As a result, the constant amplitude of shear stress of soil samples includes the shear stress induced by the membrane force. After the membrane force correction, the actual shear stress amplitude of soil should decrease with the increase of shear strain amplitude. However, in the tests of Chiaro et al.[18], the specified shear stress amplitude was monitored from the load cell after the effects of membrane force corrected. As a consequence, the shear strain of post-liquefied soil should be under-estimated compromising with the test results given by Chiaro et al.[18] under the constant shear stress amplitude. With the increase on the shear strain amplitude, the under-estimated shear strain should also increase.

2.2 Test results without the initial shear stress

As described in Table 2, specimens Nos. 1—7 were tested with zero initial static shear stress. Specimens Nos. 1—4 were tested with a constant cyclic stress amplitude of 25 kPa and a varying effective

confining pressure from 80 kPa to 150 kPa. Specimens Nos. 5—7 were tested with a constant effective confining pressure, 100 kPa, and a varying cyclic loading amplitude from 14 kPa to 30 kPa.

Fig. 8 plots the testing results of the specimen with an effective confining pressure of 100 kPa, including the pore pressure development curve (Fig. 8 (a)), the partial effective stress path (Fig. 8 (b)), and the shear stress-strain curve (Fig. 8(c)). Figs. 8(a, b) show that during the cyclic loading, the pore pressure rose quickly and approached to the magnitude of effective confining pressure, resulting in a condition of zero effective mean principle stress, i.e., full liquefaction, within three loading cycles. The state when the effective mean principle stress reached zero for the first time is defined as initial liquefaction and the number of loading cycles is defined as N_{IL}. Fig. 8(c) shows that during the cyclic loading, the shear strain accumulated continuously. The resistance against the cyclic strain accumulation was characterized by the number (N) of loading cycles required to achieve a specific amount of accumulated single-amplitude shear strain (γ_{SA}) at different cyclic stress ratios (CSR). The N-value to reach the strain accumulation up to 7.5%, 20%, 30%, 40% and 50%, is defined as $N_{7.5}$, N_{20}, N_{30}, N_{40} and N_{50}, and listed in Table 2 for each test.

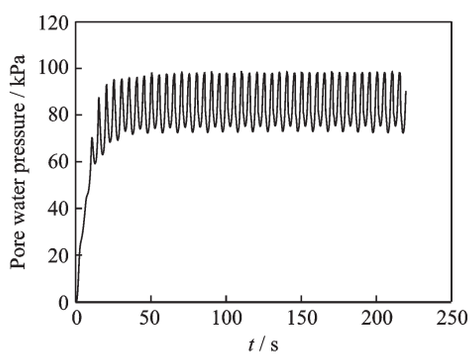

(a) Pore pressure development curve

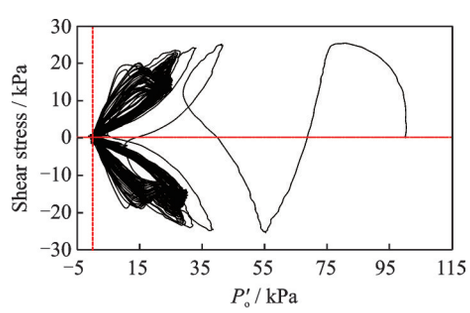

(b) Partial effective stress path

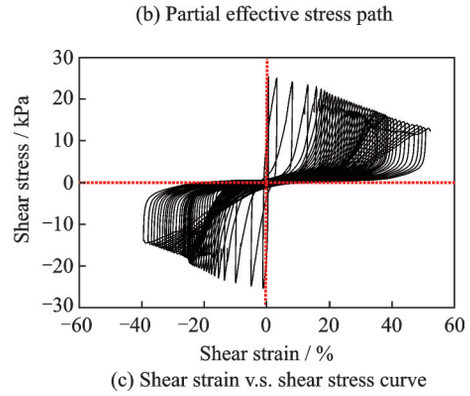

(c) Shear strain v.s. shear stress curve

Fig.8 Testing results without initial static shear stress when P'_o=100 kPa

Fig. 9 plots the variation of the resistance to initial liquefaction and cyclic strain accumulation with the effective confining stress at a constant cyclic stress amplitude of 25 kPa. Fig. 9 shows that when the initial liquefaction occurred, the accumulated single-amplitude shear strain was close to 7.5%. This finding is consistent with that of Chiaro et al.[18], who further reported that the number of loading cycles, $N_{7.5}$, to achieve a single-amplitude strain level of 7.5% in undrained cyclic torsional tests corresponded to a single-amplitude axial strain of 5% in undrained cyclic triaxial tests based on the testing results from the Toyoura sand. The cyclic strain accumulation resistance increased with the increase of the effective confining stress[18]. The increase is nonlinear. The increasing rate of the N-value increased with the increase of P'_o, showing a convex shape of the curve, when the accumulated strain was relatively small, e.g. $N_{7.5}$ and N_{20}, and decreased with the increase of P'_o, showing a concave shape of the curve when the accumulated strain was relatively large, e.g. N_{30} and N_{40}. When the effective confining stress was low (i.e. P'_o = 80 kPa), it only required

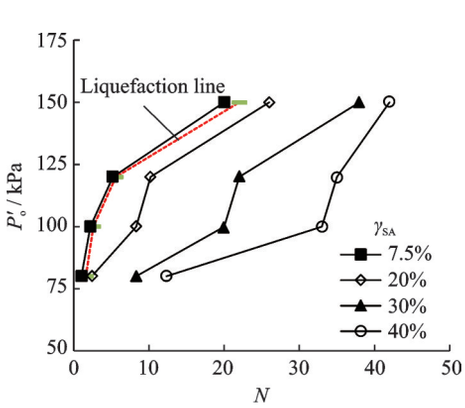

Fig.9 Relationship between N value and P'_o

about 1 to 2 loading cycles to trigger initial liquefaction after that the shear strain accumulated very fast and reached 40% within 12 loading cycles. This type of liquefaction generated rapid flow of ground and resulted in a brittle failure mode in the field. With the increase of the effective confining stress, the ground failure generally changed from brittle to ductile. When the effective confining stress reached 150 kPa, it required about 20 loading cycles to generate initial liquefaction and 42 cycles to generate 40% of the accumulated shear strain.

Fig. 10 plots the variation of the resistance to initial liquefaction and cyclic strain accumulation with the CSR when the effective confining stress was constant. In Fig.10, the cyclic strain accumulation resistance decreased with the increase of the CSR value, following a power function. The initial liquefaction occurred approximately at an accumulated single-amplitude shear strain of 7.5%. After the occurrence of the initial liquefaction, the shear strain accumulated fast and reached about 40% within about 20 to 35 loading cycles. The curves for different strain levels were almost in parallel to each other. This indicates that the CSR has a significant impact on the resistance to initial liquefaction but relatively small impact on the resistance to strain accumulation. As soon as the initial liquefaction occurred, the strain accumulation rate was not sensitive to the CSR value.

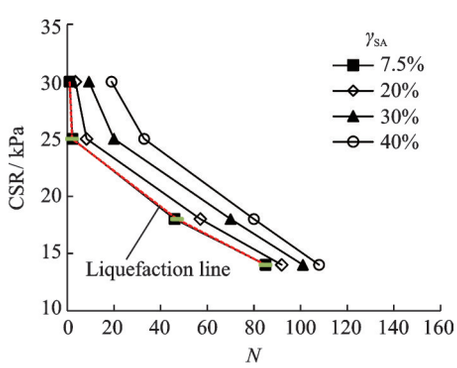

Fig.10 Relationship between N value and CSR

2.3 Effects of the initial static shear stress

In most earthquakes, liquefaction-induced large lateral ground displacements should be related to inclined ground surfaces. In other words, a soil element under an inclined ground surface has an initial static shear stress that does not exist in general for a soil element under a horizontal ground surface, as show in Fig.11. For this reason, to investigate the effect of an initial static shear stress on the post-liquefaction flow deformation of saturated sand, it is useful to understand and predict the site liquefaction-induced lateral displacement.

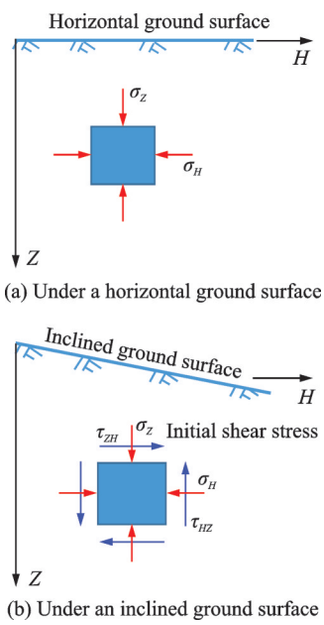

Fig.11 Initial stress condition of a soil element under different ground surfaces

Due to the normal stress condition of the soil element in slight inclined site and the buried depth of liquefiable sand, the specimens Nos. 8 to 22 were isotopically consolidated with a mean effective stress of 100 kPa and then applied with different initial static shear stresses ranging from 0 to 27 kPa. The initial SSR, defined as the ratio of initial shear stress over the mean effective principle stress, ranged from 0 to 0.27. Two series of specimens were tested, one (specimens No. 8 to 14) with a lower relative density ranging from 42.8% to 45.8% and the other (specimens Nos.15 to 22) with a higher relative density ranging from 53.1% to 55.9%.

Figs.12—14 plot the typical partial effective stress paths during the cyclic loading and the corresponding stress-strain relationship of the stress-reversal, intermediate, and non-reversal case for the set of specimens with a relative density ranging from

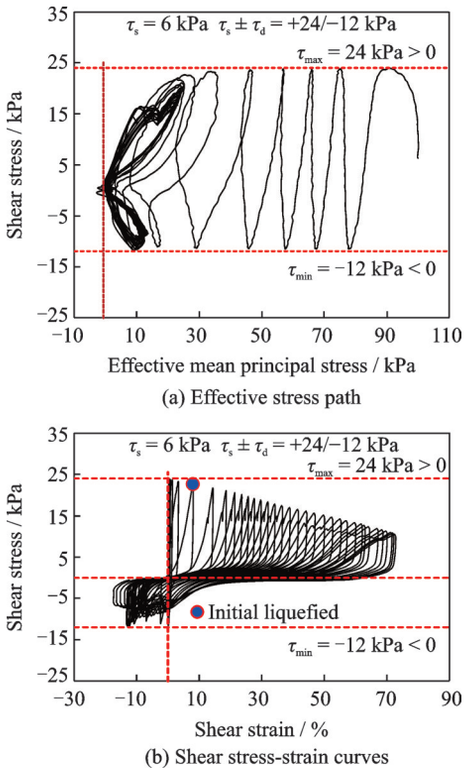

Fig.12 Testing results for stress reversal case

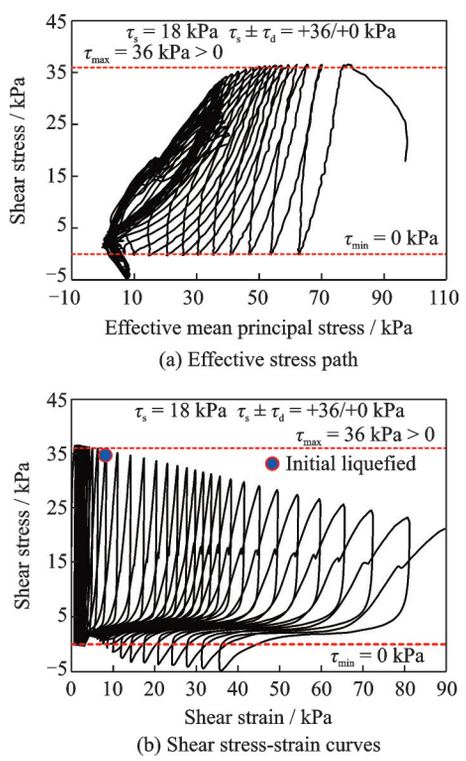

Fig.13 Testing results for intermediate case

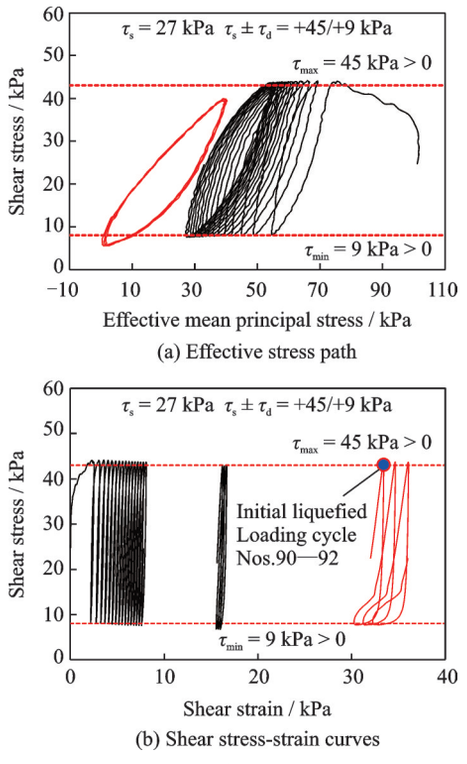

Fig.14 Testing results for stress non-reversal case

42.8% to 45.8%. In Figs.12—14, during the cyclic loading process, the effective mean principle stress gradually decreased and reached zero after a certain number of loading cycles. At the same time, the shear strain accumulated continuously. All the specimens can reach full liquefaction, i.e., zero effective mean principle stress, even for the stress non-reversal cases. However, it required a very large number of loading cycles to reach the initial liquefaction during the stress non-reversal cases. For example, it required about 90 loading cycles to reach initial liquefaction when SSR equaled 0.27, as shown in Fig.14. Similar phenomena were observed during the tests of the specimens with a higher relative density ranging from 53.1% to 55.9%. The zero effective mean principle stress occurred to all the samples and it requires 420 loading cycles to reach initial liquefaction when SSR equaled 0.2. In real earthquakes, even in very strong ones, it is less likely to generate such a large number cycles of ground motion. As such, the full liquefaction was unlikely to occur if stress reversal did not occur.

The variation of N-value for initial liquefaction and each accumulated single-amplitude shear strain with the SSR value is summarized in Table 2 and plotted in Fig.15. Fig.15 shows that during the stress reversal and intermediate cases, the initial liquefaction occurred roughly at an accumulated single-amplitude strain of 7.5%. During the stress non-reversal cases (i.e. SSR>0.18), the initial liquefac-

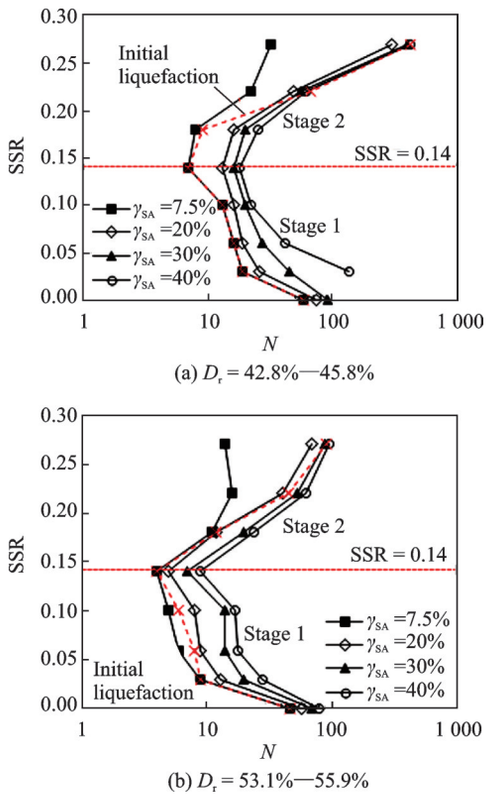

Fig.15 Relationship between SSR and number of loading cycles

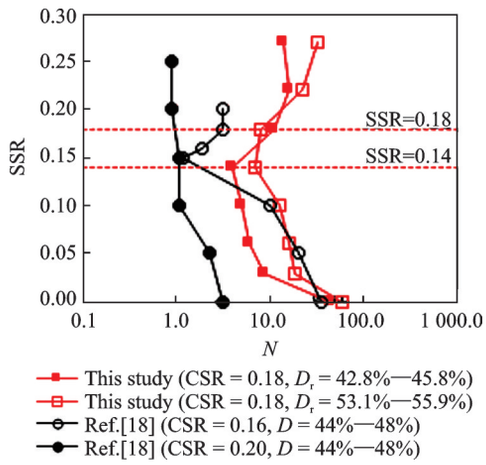

Fig.16 Comparison of cyclic strain accumulation resistance between Nanjing sand and Toyoura sand γ_{SA} = 7.5%

tion occurred at a strain larger than 7.5%. The level of strain at initial liquefaction increased with the increase of SSR and reached about 40% when SSR equaled 0.27.

Fig. 15 shows that the variation of the number of loading cycles with the SSR can be divided into two stages. During the first stage, SSR≤0.14, the number of loading cycles decreased with the increase of the SSR value. During the second stage, 0.14<SSR≤0.27, the number of loading cycles required to achieve the same accumulated single-amplitude shear strain, which generally increased as the increase of SSR, expect for one the case when SSR increased from 0.22 to 0.27. The critical point between the first and the second stages occurred when the initial shear stress is close to the amplitude of the cyclic stress. The similar rules has also been found in the test results of Toyoura sand, as shown in Fig.16. According to the test results, the particles of saturated sand should be rolling between each other under a small initial shear stress, which should make the saturated sand become looser and more apt to be liquefied. However, under a larger initial shear stress, the saturated sand should be more compacted, which induced the larger liquefaction resistance of saturated sand.

2.4 Effect of grain shape

The key physical parameters of the Nanjing sand and the Toyoura sand are listed in Table 1 for comparison. The comparison shows that the physical properties of the Nanjing sand are close to those of the Toyoura sand except for the shapes of the grains. Due to the different loading control methods, some indirect comparisons on the test results of two kind of sands are analyzed. Fig.16 plots the required number of loading cycles to generate the accumulated single-amplitude shear strain of 7.5%, 20% and 50%, for the Nanjing sand and the Toyoura sand. All the specimens were isotopically consolidated with an effective confining pressure of 100 kPa before applying initial static shear stress.

Fig.16 shows that the variation patterns of the number of loading cycles required to generate the same single-amplitude strain were consistent for both sands. The number of loading cycles first decreased and then increased with the increase of SSR. The transformation point was near the state when the initial static shear stress equaled to the cyclic shear stress amplitude.

When the initial static shear stress was zero, i.e., SSR=0, in general, the strain accumulation resistance of the Nanjing sand was higher than that

of the Toyoura sand. Fig. 16 shows that it required 46 loading cycles to generate 7.5% of accumulated strain for the Nanjing sand at relative density of 42.8%—45.8% and CSR = 0.18, compared with 35 loading cycles for the Toyoura sand at relative density of 44%—48% and CSR = 0.16. The Nanjing sand had a lower relative density and higher CSR value than the Toyoura sand, but it required more loading cycles than the Toyoura sand to generate 7.5% of accumulated strain. As shown in Fig. 15, initial liquefaction approximately occurred at an accumulated strain of 7.5%. Due to the negligible effect of under-estimated shear strain under the small shear strain amplitude mentioned in Section 2.1, the initial liquefaction resistance of the Nanjing sand was higher than that of the Toyoura sand when SSR=0. It is probably because the Nanjing sand is composed of angular grains, which results in better particle interlocking and higher shear resistance than the rounded grains of the Toyoura sand.

Fig. 16 shows that when the initial static SSR increased from zero to a small value, i.e. 0.03, the number of loading cycles required to generate 7.5% of single-amplitude shear strain of the Nanjing sand decreased much faster than that of the Toyoura sand. This indicates that the sand composed of angular grains suffers larger loss of liquefaction resistance to the small initial static shear stress than the sand composed of rounded grains, which proves that the granular structure of the angular sand should be more sensitive to the initial static shear stress. However, as SSR continuously increased, the initial static shear stress had a smaller effect on the strain accumulation resistance of the Nanjing sand than that of the Toyoura sand. Fig.16 shows that when the initial static SSR approached or exceeded the CSR (SSR$\geqslant$0.14), the resistance of the Nanjing sand to the initial liquefaction was stronger than that of the Toyoura sand. The number of loading cycles to generate 7.5% of single-amplitude shear strain, also initial liquefaction, of the saturated Nanjing sand was larger than that of the Toyoura sand. That is because the Nanjing sand with angular grains can be more compacted than that of the Toyoura sand with rounded grains under a larger initial static shear stress.

3 Conclusions

This paper mainly investigates the effects of initial static shear stress and grain shape on liquefaction of the saturated Nanjing sand under torsional shear. The Nanjing sand, mainly composed of platy grains, is tested with different initial static SSRs using a hollow column torsional shear apparatus. Some conclusions are drawn as follows.

(1) For the stress reversal and intermediate cases, the initial liquefaction occurs approximately at an accumulated single-amplitude shear strain of 7.5%. For the stress non-reversal cases, it requires a very large number of loading cycles to reach full liquefaction if stress reversal does not occur, and the initial liquefaction occurs at a much higher single-amplitude accumulated shear strain. Considering in real earthquakes, even in very strong ones, it is less likely to generate such a large number cycles of strong ground motion. As such, the full liquefaction is unlikely to occur during real earthquakes. To this view, with the increasing initial static stress, the large deformation of the Nanjing sand should be mainly induced by the cyclic liquefaction firstly under a smaller initial shear stress, and then be induced by the residual deformation failure.

(2) The number of loading cycles requires to generate a specific level of accumulated single-amplitude shear strain decreases with the increase of SSR when the SSR is relatively low but increases with the increase of SSR when the SSR is relatively high. The critical point occurs approximately when the initial shear stress is close to the amplitude of cyclic loading. To explain this finding, the particles of the saturated sand should be rolling between each other under a smaller initial shear stress, which should make the saturated sand become looser and more apt to be liquefied. However, under a larger initial static shear stress, the saturated sand should be more compacted, which should induce the larger liquefaction resistance of sand.

(3) Comparison of testing results between the Nanjing sand composed of platy grains and the Toy-

oura sand composed of rounded grains shows that grain angularity increases the liquefaction resistance when the saturated sand is isotopically consolidated. A small initial static shear stress causes larger loss of liquefaction resistance for angular sand than the rounded sand. Under a larger initial static shear stress, the Nanjing sand with angular grain can be compacted more easily, and then it has a stronger stiffness to resist the large residual deformation failure.

Note: All data included in this study are available upon request by contact with the corresponding author.

References

[1] HAMADA M, YASUDA S, ISOYAMA R, et al. Observation of permanent ground displacements induced by soil liquefaction[J]. Proceedings of the Japan Society of Civil Engineers, 1986, 13(6): 211-220.

[2] YOUD T L, PERKINS D M. Mapping of liquefaction severity index[J]. Journal of Geotechnical Engineering, 1987, 113(11): 1374-1392.

[3] HAMADA M, O'Rourke T D. Large ground deformations and their effects on lifelines: 1964 Niigata earthquake, case studies of liquefaction and lifelines performance during past earthquake[J]. Japanese Case studies, 1992, 1(3):1-3, 123.

[4] SASAKI Y, TOKIDA K, MATSUMOTO H, et al. Shake table tests on lateral ground flow induced by soil liquefaction[C]// Proceedings of the 3rd Japan-US Workshop on Earthquake Resistant Design of Lifeline Facilities and Countermeasures for Soil Liquefaction. Suny-Buffalo, Buffalo: National Center for Earthquake Engineering Research, 1991:371-385.

[5] TABOADA V M, ABDOUN T, DOBRY R. Prediction of liquefaction-induced lateral spreading by dilatant sliding block model calibrated by centrifuge tests[C]// Proceedings of the 11th World Conference on Earthquake Engineering. Pergamon, Oxford, U.K.: [s.n.], 1996: 376.

[6] ELGAMAL A W, ZEGHAL M, TABOADA V M, et al. Analysis of site liquefaction and lateral spreading using centrifuge model tests[J]. Soils and Foundation, 1996, 36(2): 111-121.

[7] ABDOUN T, BENNETT V, DOBRY R, et al. Full-scale laboratory tests using a shape-acceleration array system[C]// Proceedings of the 4th Decennial Geotechnical Earthquake Engineering and Soil Dynamics Conference. Reston, VA. USA: [s.n.], 2008.

[8] LEE K L, SEED H B. Cyclic stress conditions causing liquefaction of sand[J]. Journal of Soil Mechanics & Foundations, 1967(4): 47-70.

[9] ISHIHARA K. Liquefaction and flow failure during earthquakes[J]. Geotechnique, 1993, 43(3): 351-451.

[10] VAID Y P, STEDMAN J D, SIVATHAYALAN S. Confining stress and static shear effects in cyclic liquefaction[J]. Canadian Geotechnical Journal, 2001, 38(3): 580-591.

[11] YANG Z X, PAN K. Flow deformation and cyclic resistance of saturated loose sand considering initial static shear effect[J]. Soil Dynamics and Earthquake Engineering, 2017, 92: 68-78.

[12] TOWHATA I, SASAKI Y, TOKIDA K, et al. Prediction of permanent displacement of liquefied ground by means of minimum energy principle[J]. Soils and Foundation, 1992, 32(3): 97-116.

[13] ZHANG J M, WANG G. Large post-liquefaction deformation of sand, part I: Physical mechanism, constitutive description and numerical algorithm[J]. Acta Geotechnica, 2012, 7(2): 69-113.

[14] KERAMATIKERMAN M, CHEGENIZADEH A. Effect of particle shape on monotonic liquefaction: Natural and crushed sand experimental mechanics[J]. Experimental Mechanics, 2017, 57(8): 1341-1348.

[15] VAID Y P, LIAM F W D. Static shear and liquefaction potential[J]. Journal of Geotechnical Engineering Division, 1979, 105(10): 1233-1246.

[16] YOSHIMINE M, ROBERTSON P K, WRIDE C E. Undrained shear strength of clean sands to trigger flow liquefaction[J]. Canadian Geotechnical Journal, 1999, 36(5): 891-906.

[17] YOSHIMI Y K, OH-OKA H. Influence of degree of shear stress reversal on the liquefaction potential of saturated sand[J]. Soils and Foundation, 1975, 15(3): 498-510.

[18] CHIARO G, KOSEKI J, SATO T. Effects of initial static shear on liquefaction and large deformation properties of loose saturated Toyoura sand in undrained cyclic torsional shear tests[J]. Soils and Foundation, 2012, 52(3): 498-510.

[19] ROBERTSON P K, WRIDE C E. Evaluating cyclic liquefaction potential using the cone penetration test[J]. Canadian Geotechnical Journal, 1998, 35(3): 442-459.

[20] ROBERTSON P K. Estimation of minimum undrained shear strength for flow liquefaction using the CPT[C]// Proceedings of the 2nd International Conference on Earthquake Geotechnical Engineering. Balkema, Rotterdam, The Netherlands: [s. n.], 1999: 21-25.

[21] IDRISS I M, BOULANGER R W. Soil liquefaction during earthquakes[M]. [S.l.]: Earthquake Engineering Research Institute (EERI), 2008.

[22] SEED H B. Landslides during earthquakes due to soil liquefaction[J]. Journal of the Soil Mechanics and Foundation Division, 1968, 94(5): 1055-1122.
[23] VAID Y P, CHERN J C. Effect of static shear on resistance to liquefaction[J]. Soils and Foundation, 1983, 23(1): 47-60.
[24] YANG J, SZE H Y. Cyclic behaviour and resistance of saturated sand under non-symmetrical loading[J]. Geotechnique, 2011, 61(1): 57-73.
[25] KOERNER R M. The behavior of cohensionless soils formed from various minerals[D]. Durham: Duke University, 1968.
[26] ISHIBASHI I, SHERIF M A, CHENG W L. The effects of soil parameters on pore-pressure-rise and liquefaction prediction[J]. Soils and Foundation, 1982, 22(1): 39-48.
[27] VAID Y P, CHERN J C, TUMI H. Confining pressure, grain angularity, and liquefaction[J]. Journal of Geotechnical Engineering, 1985, 110(10): 1229-1235.
[28] PAYAN M, KHOSHGHALB A, SENETAKIS K. Effect of particle shape and validity of Gmax models for sand: A critical review and a new expression[J]. Computers and Geotechnics, 2016, 72: 28-41.
[29] MOHAMMADNIA M, MIRGHASEMI A A. Particle shape consideration in DEM triaxial test simulations[C]// Proceedings of International Conference on Discrete Element Methods. Singapore: Springer, 2016.
[30] CHEN G X, ZHOU E L, PAN H, et al. The influence of undrained cyclic loading patterns and consolidation states on the deformation features of saturated fine sand over a wide strain range[J]. Engineering Geology, 2016, 204: 77-93.
[31] DEGREGORIO V B. Loading systems, sample preparation, and liquefaction[J]. Journal of Geotechnical Engineering, 1990, 116(5): 805-821.
[32] HYODO M, TANIMIZU H, YASUFUKU N, et al. Undrained cyclic and monotonic triaxial behavior of saturated loose sand[J]. Soils and Foundation, 1994, 34(1): 19-32.

Acknowledgements This work was supported by the National Natural Science Foundation of China (Nos. 51778290, 51778386), the National Science Fund for Distinguished Young Scholars (No. 51725802), and the Natural Science Foundation of Jiangsu High School (No. 16KJA560001).

Author Prof. **ZHUANG Haiyang** received his B.S.degree in civil engineering and Ph.D. degree in geotechnical engineering from Nanjing Tech University in 2000 and 2006, respectively. Since 2006, he has been working at Nanjing Tech University. And now he is a full professor at the College of Transportation Science & Engineering, Nanjing Tech University. His research interests include soil dynamics, soil-isolated structure interaction and deep excavation of soil foundation.

Author contributions Prof. **ZHUANG Haiyang** and Prof. **YU Xu** conceived and supervised this project. Mr. **PAN Shuxuan** wrote the manuscript. Dr. **LIU Qifei** contributed to the tests. All authors commented on the manuscript draft and approved the submission.

Competing interests The authors declare no competing interests.

(Production Editor: ZHANG Tong)

初始静剪应力和颗粒形状对南京砂液化特性的影响

庄海洋[1], 潘书轩[1], 刘启菲[1], 于 旭[2]
(1.南京工业大学岩土工程研究所, 南京 210009, 中国; 2.南京工程学院建筑工程学院, 南京 211167, 中国)

摘要:基于南京砂的片状颗粒特殊性,采用循环空心圆柱扭剪仪,开展了扭剪受力状态下初始静剪应力和颗粒形状对南京砂液化特性的试验研究。结果表明:无论是在双向循环加载和单向循环加载,南京砂土在较大的初始静剪应力条件下都能达到完全液化状态。总体来看,在单向循环加载条件下,南京砂要达到完全液化状态所需的循环加载次数明显增加。随着初始静剪应力的增加,引起南京砂土动力大变形的主要诱因由较小初始剪应力状态下的循环液化为主逐渐转化为较大初始剪应力状态下的循环累积变形为主,上述动力大变形机理转化的临界状态为初始静剪应力接近循环加载幅值的状态。此外,在零初始剪应力状态下,与圆粒砂相比,南京砂的片状颗粒形状有助于提高其抗液化能力,但很小的初始静剪应力将会大大降低南京砂的抗液化能力。在较大的初始静剪应力条件下,片状南京砂具有更大的抵抗累积大变形的能力。

关键词:南京砂;砂土液化;初始剪应力;颗粒形状;累积变形破坏